Oblique impact dynamics of micron particles onto a liquid surface

Bingqiang Ji, Zuozhou Tang, and Qiang Song*

Key Laboratory of Thermal Science and Power Engineering of Ministry of Education, Department of Energy and Power Engineering, Tsinghua University, 100084 Beijing, China

(Received 19 September 2019; accepted 4 November 2020; published 30 November 2020)

Micron particles rotate and their trajectories deviate from the impact direction when impacting the liquid surface obliquely; thus their impact dynamics is largely different from that of vertical impact, which remains to be studied in depth. In this study we established a three-dimensional simulation method by solving the coupled equations of particle motion and fluid flow and adopting a dynamic meshing technique and slip velocity boundary condition that accurately reproduced the particle motion and gas-liquid interface evolution during oblique impact. Our results, based on detailed flow field and acting forces and moments analyses, demonstrate that the particle's nonaxisymmetric wetting leads to the nonaxisymmetric distribution of fluid pressure and shear stress along the particle surface, and thus deviates the dominating forces at different impact stage from its direction of motion, which makes the particle trajectory deviate from the impact direction and also generates a viscous moment that rotates the particle. We also illustrate how the impact angle and Weber number modulate the flow field around the particle as well as the acting forces and finally influence the particle motions. These findings provide a deep understanding of the dynamics of the nonaxisymmetric impact of the micron particle on liquid surfaces, which is a ubiquitous scenery in nature and industry.

DOI: 10.1103/PhysRevFluids.5.114006

I. INTRODUCTION

The impact of objects on liquid surfaces occurs widely in nature and industry. This phenomenon was initially studied by the military, including the water entry of air-to-sea weapons (bullets and bombs) [1,2] and the water landing of aircraft and spacecraft [3,4]. This is also of significant interest in the field of bionics for understanding the floating, walking, and jumping of aquatic insects on liquid surfaces [5–8]. Particles impacting liquid surfaces are common in mineral flotation when screening mineral particles with different properties [9] and in jet metallurgy when preparing particle-reinforced metal matrix composites [10]. The impact behavior of micron particles determines the particle capture efficiency in wetting scrubbing (and wetting deposition in nature) [11–13]. Therefore the study of particles impacting liquid surfaces is helpful for understanding related natural phenomena and providing guidance to related industrial processes.

The vertical impact of spherical particles on liquid surfaces has been of primary interest in related studies. This process can be considered axisymmetric and is determined by the dimensionless parameters of the Weber number We $(=\rho_l {u_0}^2 d_p/\sigma)$, the Reynolds number Re $(=\rho_l u_0 d_p/\mu_l)$, the Bond number Bo $(=\rho_l {d_p}^2 g/\sigma)$, the density ratio $D\,(=\rho_s/\rho_l)$, and the contact angle θ, where ρ_l, μ_l, and σ are the density, viscosity, and surface tension coefficient of the liquid, respectively, u_0 is the impact velocity, d_p and ρ_s are the diameter and density of the particle, respectively, and g is the

*qsong@tsinghua.edu.cn

gravitational acceleration. Large particles with $Bo \gg 1$ may exhibit two impact modes of oscillation and submergence after impact under the influence of gravity, buoyancy, and hydrodynamic forces [14]. The effect of the surface tension force becomes significant with the decrease in the particle size [15], causing a millimeter-sized particle with $\text{Bo} \sim 1$ demonstrating three impact modes of oscillation, rebound, and submergence [16]. A particle's impact causes different cavity shapes in the gas-liquid interface [17]. A quasistatic cavity forms when We is small [18], while a deeper cavity is produced due to the pinning of the three-phase contact line (TPCL) during impact with a large We [19]. For the vertical impact of millimeter-sized particles, the dynamics of particle motion and gas-liquid interface evolution were investigated theoretically, numerically, and experimentally. The effects of impact parameters such as the particle wettability, density ratio, and Weber number were revealed, and criteria for distinguishing different impact modes were proposed [18,20,21]. For micron particles in industrial processes such as mineral flotation and wet scrubbing, the effect of gravity on their impact behavior can be safely neglected because $Bo \gg 1$, thus demonstrating different impact behaviors compared to large particles. Our previous work investigated the dynamics of a micron particle's vertical impact on liquid surfaces and found that the initial and late stages are dominated by the hydrodynamic force and surface tension force, respectively [22–24]. The characteristics of particle motion and gas-liquid interface evolution were illustrated, and the energy conversion mechanism was revealed.

Particles impact liquid surfaces at arbitrary angles in practical situations. Most children know how to skip a stone on a lake [25,26]. When a large sphere impacts a liquid surface with high velocity, it will rebound if the impact angle is less than a critical value because a large upward component of the hydrodynamic force is produced due to nonaxisymmetric wetting along its motion direction [27]. The trajectory of a streamlined body is no longer straight when the instability of exerted torques (including Archimede's and hydrodynamic) is triggered by the deviation of the center of mass (Guillet *et al.* [28]). However, at present, little is known about the oblique impact of micron particles, where the surface tension force plays a key role and the gravity effect can be totally neglected compared to that of large bodies. Our previous work experimentally studied the oblique impact of poly(methyl methacrylate) (PMMA) microspheres on a liquid surface and found that different from the vertical impact, the particle trajectory will deviate from its impact direction and the particle will rotate during oblique impact [29]. However, particle rotation cannot be measured quantificationally due to experimental limitations, and it is difficult to give deep insights into the behind dynamics of the particle rotation and trajectory deviation based on the experimental observation, which is very important for the modeling and prediction of particle impact behaviors. As an important research method, numerical simulation has been widely used to study interfacial multiphase flow problems, including objects impacting a liquid surface [30,31]. Therefore it is necessary to investigate the oblique impact of micron particles with a detailed numerical simulation to reveal the dynamics of the particle rotation and trajectory deviation and the role of the impact parameters.

In this study we develop a three-dimensional simulation method for research into a micron particle's oblique impact. Equations of particle motion and fluid flow are solved with a dynamic meshing technique and slip velocity boundary condition. The simulation accuracy is verified with experimental data at different impact angles. Particle motions that are difficult to capture experimentally, such as particle rotation, TPCL motion, and capillary wave propagation, are reported. The evolution of the dominant forces and moments are analyzed, and the effects of the impact angle and Weber number on the impact dynamics are investigated.

II. GOVERNING EQUATIONS AND NUMERICAL METHODS

When a rigid spherical particle impacts a horizontal liquid surface with an inclination angle of α and a translational velocity of $\boldsymbol{u_0}$, the gas-liquid surface distorts as shown in Fig. 1, where s is the particle displacement, h is the vertical displacement of the particle, $\boldsymbol{u}$ is the particle's translational velocity, $\boldsymbol{\omega}$ is the particle's rotational velocity, α_u is the inclination of $\boldsymbol{u}$ relative to the horizontal

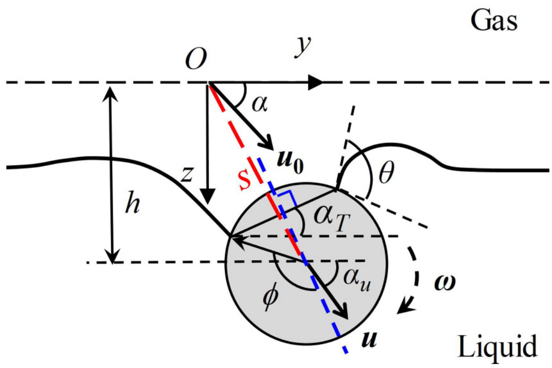

FIG. 1. Schematic of a micron particle impacting a liquid surface.

plane, ϕ is the angular position of the TPCL, and α_T is the inclination of the TPCL. The coordinate origin is set as the particle's center when it contacts the liquid surface, and the yz plane is set as the vertical plane where $\boldsymbol{u_0}$ is located, which is also the symmetry plane of the impact.

A. Equations of fluid flow and particle motion

Since the velocity of the fluid is much smaller than the local speed of sound, the fluid is assumed to be incompressible. The mass conservation equation and Navier-Stokes equation of the fluid are as follows:

$$\frac{\partial \rho}{\partial t} + \nabla \cdot \rho \boldsymbol{v} = 0, \tag{1}$$

$$\frac{\partial (\rho \boldsymbol{v})}{\partial t} + (\boldsymbol{v} \cdot \nabla)\rho \boldsymbol{v} = -\nabla p + \nabla \cdot \left[\mu(\nabla \boldsymbol{v} + \nabla \boldsymbol{v}^{\mathrm{T}})\right] + \rho \boldsymbol{g} + \boldsymbol{f}_{\mathbf{st}}, \tag{2}$$

where t is the time, ρ is the fluid density, $\boldsymbol{v}$ is the fluid velocity, p is the pressure, μ is the dynamic viscosity of the fluid, and $\boldsymbol{g}$ is the gravitational acceleration. The two-phase flow of the gaseous and liquid phases is calculated using the volume-of-fluid method as described by Hirt and Nichols [32]. The volume fraction of each phase in each cell is defined in this method, and the density and viscosity of the fluid near the gas-liquid interface is calculated by interpolation. $\boldsymbol{f}_{st}$ is the volumetric surface tension force, and it exists only in the gas-liquid interface and is counted with the continuum surface force (CSF) model [33]. The related equations were presented in our previous work [23].

The translational and rotational motions of the particle change under the influence of the acting forces and moments by the liquid and interface during impact. According to Newton's second law, the equation of particle motion can be expressed as

$$m_p \frac{d\boldsymbol{u}}{dt} = \boldsymbol{F}_f + \boldsymbol{F}_{\mathrm{s}} + \boldsymbol{F}_{\boldsymbol{g}}, \tag{3}$$

$$I_p \frac{d\omega}{dt} = \boldsymbol{M}_f + \boldsymbol{M}_s + \boldsymbol{M}_{\boldsymbol{g}}, \tag{4}$$

where m_p and I_p are the mass and moment of inertia of the particle, respectively. $\boldsymbol{F}_f$, $\boldsymbol{F}_s$, and $\boldsymbol{F}_{\boldsymbol{g}}$ are the fluid force, surface tension force, and gravity acting on the particle, respectively. $\boldsymbol{M}_f$, $\boldsymbol{M}_s$, and $\boldsymbol{M}_{\boldsymbol{g}}$ are the moments produced by these three forces, which were calculated by $\boldsymbol{M} = \boldsymbol{r} \times \boldsymbol{F}$, where $\boldsymbol{r}$ is the distance vector of the acting point of the corresponding force to the particle's rotation axis.

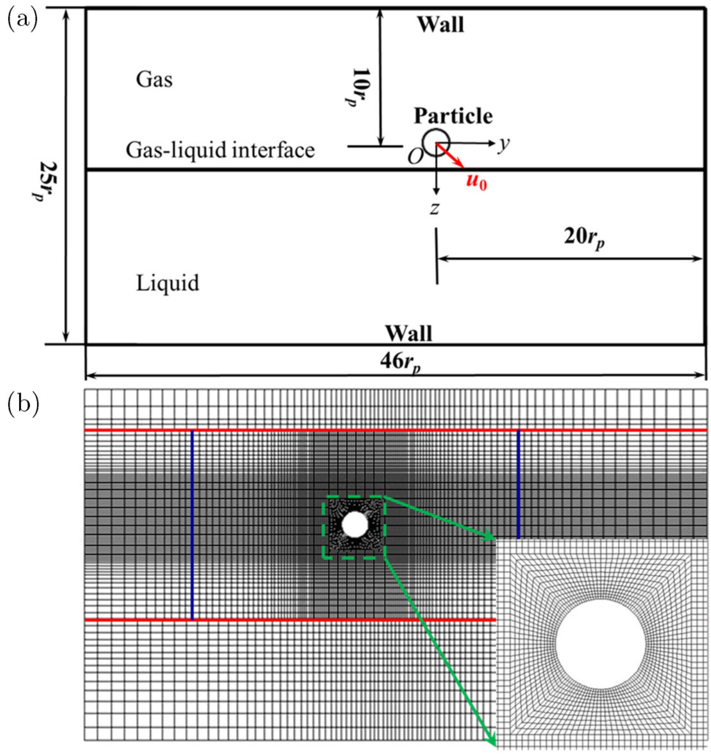

FIG. 2. Illustrations of (a) the computational domain and (b) the mesh at the symmetric plane.

$\boldsymbol{F}_f$ is computed as the integral of the pressure stress and viscous stress over the entire particle surface area A_p:

$$\boldsymbol{F}_f = \iint_{A_p} -p\mathbf{n}_s dA + \iint_{A_p} \mu(\nabla \boldsymbol{v} + \nabla \boldsymbol{v}^{\mathrm{T}}) \cdot \boldsymbol{n}_s dA, \tag{5}$$

where $\boldsymbol{n}_s$ is the unit normal vector of the sphere surface. $\boldsymbol{F}_s$ is calculated as

$$\mathbf{F}_s = \int_{TPCL} \sigma \varepsilon dl, \tag{6}$$

where $\boldsymbol{\varepsilon}$ is the unit interface direction vector at the TPCL. The gravity is computed by $\boldsymbol{F}_g = m_p \boldsymbol{g}$ and acts on the centroid of the particle. Thus $\boldsymbol{M}_g = 0$.

B. Numerical methods

Because the fluid flow is symmetric along the yz plane during impact, the particle always moves on the yz plane and rotates along the x direction, and a three-dimensional symmetric computational domain is adopted. The reasonable domain, mesh sizes, and time steps are determined by an independent analysis. As shown in Fig. 2, the computational domain length is $20r_p$ (r_p is particle radius) in the x direction. A structured mesh with a local mesh refinement in proximity to the particle is utilized. The total cell number is 826 400 cells with a corresponding minimum mesh size of $r_p/60$. A variable time step is adopted to ensure a global Courant number of less than 0.2.

A no-slip velocity boundary condition and a constant contact angle of 90° are set for the domain boundary. Since the adopted dynamic meshing technique (introduced in the following) only considers the particle's translation movement, a slip velocity boundary is adopted for the particle boundary to couple the particle's rotational movement with the fluid flow, which represents the no-slip boundary of a rotating particle in the practical situation. The slip velocity equals the velocity of the particle surface caused by the particle's rotation and is expressed as

$$\boldsymbol{v_w} = \boldsymbol{\omega} \times \boldsymbol{r_w}, \tag{7}$$

where $\boldsymbol{r_w}$ is the vector from the sphere center to the considered position on the particle surface. Although the contact angle between the particle and TPCL dynamically changes during the sinking process, experimental research on the impact of small hydrophobic spheres found that the difference between the dynamic contact angle and static contact angle is very small throughout most of the sinking process [22]. Simulation research by Ding *et al.* [19] and Kintea *et al.* [15] showed that a constant contact angle can also capture the dynamics of the particle and gas-liquid interface. Therefore we adopt a constant advancing contact angle θ for the particle wall in this study.

As a dynamic meshing technique, the layering scheme is adopted to reconstruct the mesh to couple the particle's translational movement with the fluid flow. As shown in Fig. 2(b), the mesh is divided into five parts by four interfaces. The cells in the middle part remain unchanged and move in the yz plane together with the particle, whereas the cells in the left and right parts move at the velocity of the particle in the z direction. The cells adjacent to the interface in the left, right, top, and bottom parts are compressed or stretched. When a cell is stretched or compressed to a certain extent, it splits into two cells or merges with its adjacent cell to ensure that all the grids are structured. In this way, the mesh reconstruction in each time step is realized.

The gaseous and liquid phases are initially still when the particle moves from the gaseous phase to the gas-liquid interface at a translational velocity of $\boldsymbol{u_0}$ without rotation in the position $2r_p$ above the gas-liquid interface. The detailed computational procedure was reported in our previous work [23]. The physical parameters of the gaseous phase are specified as the physical parameters of air at a normal temperature and pressure. We set $\rho_l = 998.2\,\mathrm{kg/m^3}$, $\sigma = 0.0728\,\mathrm{N/m}$, $\mu_l = 0.001\,\mathrm{Pa\,s}$, $\rho_s = 1180\,\mathrm{kg/m^3}$, $\theta = 110^\circ$, $d_p = 306.0\,\mu\mathrm{m}$, and $u_0 = 2.84\,\mathrm{m/s}$ as default parameters. Thus We = 34 and $D = 1.18$. The impact angle α varies between 15° and 90° to investigate the effect of the impact angle. The We number varies between 10 and 50, while Re is fixed at 867 by adjusting u_0 and μ_l to investigate the effect of We.

III. RESULTS AND DISCUSSION

A. Motion behaviors

An impact process ($\alpha = 43.8^\circ$, We = 34, and Re = 867) observed by the experiment [29] is numerically simulated first, and the obtained particle trajectory is shown in Fig. 3(a), where $T = tu_0/d_p$ represents the dimensionless time and $T = 0$ is the moment when the particle contacts the liquid surface. The particle moves along its impact direction first after impact and then the trajectory deviates significantly with respect to its impact direction and eventually submerges at $z \approx 2d_p$ and $T \approx 5.8$. Figure 3(b) demonstrates the evolution of the deviation of the particle trajectory to its impact direction (Δs). It shows that the particle's trajectory deviates slightly upward at the initial stage and then obviously deviates downward. The particle's maximum trajectory deviation (Δs_m) before the liquid surface pinches off is approximately $0.2d_p$. The numerical simulation accurately predicts the particle's trajectory, the evolution of the particle displacement with time, and the location and time when the particle is submerged. Although the particle's rotation during impact can be deduced by the movement of the small bubble attached above the particle after it submerges, it cannot be directly measured by the experiment [29]. Figure 3(b) shows the variation in the particle's angular velocity with time during impact obtained numerically. The particle rotates clockwise (topspin) after impacting the gas-liquid interface without rotation, and the angular velocity first increases and then decreases. The maximum angular velocity is 913 rad/s. By comparing the experimentally measured angular velocity after the particle is submerged, we can conclude that the numerical simulation accurately captures the rotation of the particle during impact.

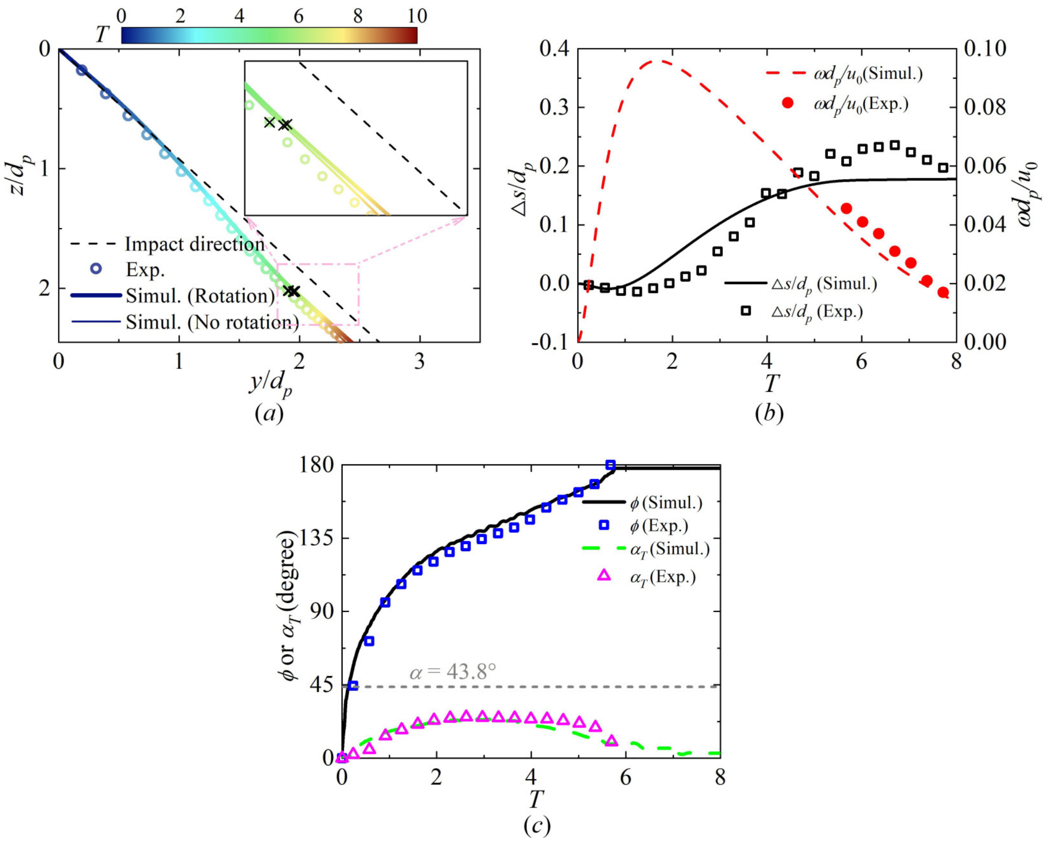

FIG. 3. Comparison of (a) the particle trajectory colored based on the dimensionless time $T\,(=tu_0/d_p)$, with $\times$ representing the position where the particle is submerged, (b) the particle's trajectory deviation Δs (the positive value means the particle's trajectory deviates downward) and rotational angular velocity ω, and (c) the evolution of the angular position of the TPCL ϕ and the inclination of the TPCL plane α_T between the simulations and experiments [29]: $\alpha = 43.8^\circ$, $d_p = 306.0\,\mu$m, $u_0 = 2.84$ m/s, We = 34, and Re = 867. The black dashed line in (a) represents the impact direction, while the inset figure plots the enlarged view near the particle submerged position.

Figure 4 presents the time series of the gas-liquid interface obtained numerically and experimentally. It shows that the liquid surface shape in the yz plane calculated numerically matches the experimental results extremely well. The gas-liquid interface distortion caused by the particle's impact is nonaxisymmetric, and the TPCL on the left side of the particle first moves below the undisturbed liquid surface compared to that on the right, causing the cavity to evolve from a half cavity to a full cavity. The assumption of constant contact angle results in the TPCL being located in a plane (the TPCL plane) during impact in simulation, which is also observed by the experiment and confirms the rationality of the constant contact angle assumption. Figure 3(c) provides a comparison of the evolution of the angular position of the TPCL and the TPCL inclination between simulations and experiments [26], which shows that the numerical simulation accurately reproduces the experimental results. The numerical simulation also captures the propagation of the capillary wave around the particle that is difficult to observe in the experiment and presents a three-dimensional comprehensive observation of the impact process. Figure 4 shows the propagation of the capillary wave after impact in the top view. As the particle sinks, the rim outside the cavity spreads away from the particle. The propagation speed and peak of the rim in front of the particle are larger than

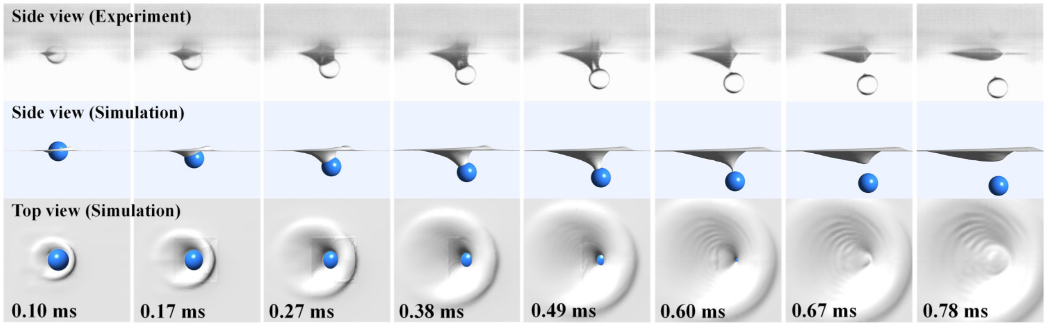

FIG. 4. Time series of the gas-liquid interface obtained numerically and experimentally [29]: $\alpha = 43.8^\circ$, $d_p = 306.0\,\mu\text{m}$, $u_0 = 2.84\,\text{m/s}$, We = 34, and Re = 867.

those behind the particle due to the particle's lateral velocity. The difference in the capillary wave propagation around the particle during oblique impact makes the cavity nonaxisymmetric along the particle velocity direction, and the slip velocity of the TPCL on the particle surface is different, which demonstrates that the TPCL plane is not perpendicular to the particle velocity direction and inclines to the horizontal plane. Thus, the particle's wetting is nonaxisymmetric along its velocity direction during oblique impact.

To explore the effect of the impact angle on the motion behavior and further verify the applicability of the numerical method, we numerically calculate the impact processes of $\alpha = 15^\circ$, 30°, 45°, 60°, 75°, and 90° when We = 34 and Re = 867. Particles with $\alpha = 15^\circ$ exhibit an oscillation mode, where the particle cannot pierce the liquid surface to submerge, and then oscillate and finally float at the liquid surface. Particles with $\alpha \geqslant 30^\circ$ exhibit a submergence mode, where the particle can pierce the liquid surface and finally submerge into the liquid. Here we define the penetration depth h_p as either the maximum z coordinate that is reached by the oscillating particle or the z coordinate of the submerging particle at the moment that the cavity pinches off and the particle submerges. Figure 5(a) shows the penetration depth (h_p) and maximum trajectory deviation (Δs_m) of the particles as a function of α. The penetration depth of the submerged particle is approximately $2d_p$ and decreases slightly with the decrease in α, and the maximum deviation of the particle trajectory increases with the decrease in α, which is consistent with the experimental results [29]. The variations in the maximum angular velocity of the particles (ω_m) and the maximum inclination of the TPCL plane (α_{Tm}) with α are presented in Fig. 5(b). The smaller the α, the larger the $\omega_m d_p/u_0$, indicating that the rotation of the particles during impact is more significant. α_{Tm} increases as α decreases and $\alpha_{Tm} < 90^\circ - \alpha$ at all impact angles. As α decreases, the angle between the TPCL plane and the particle equatorial plane ($90^\circ - \alpha - \alpha_{Tm}$) increases, which demonstrates a larger tilting of the TPCL plane with respect to the direction of motion, representing a larger wetting nonaxisymmetry. The numerical simulation accurately captures the particle motion and the gas-liquid interface evolution during impact with different impact angles, indicating the accuracy and applicability of the numerical method.

The impact processes of We = 10, 20, 30, 40, and 50 when $\alpha = 45^\circ$ and Re = 867 are simulated to illustrate the effect of Weber number (or the role of inertia) on the motion behavior of the micron particle. Particles with We = 10 and 20 exhibit an oscillation mode, while particles with We = 30, 40, and 50 exhibit a submergence mode. Figure 5(c) illustrates the penetration depth (h_p) and maximum trajectory deviation (Δs_m) of the particles as a function of We. The penetration depth increases with increasing We for the oscillating particles and remains constant for submerged particles with the same α, which is consistent our previous experimental findings [29]. The maximum deviation of the particle trajectory increases with increasing We and, interestingly, becomes negative when We is small (We = 10, for example), which means the particle's downward trajectory deviation at the late impact is weaker than its upward trajectory deviation at the initial impact. Figure 5(d) depicts the

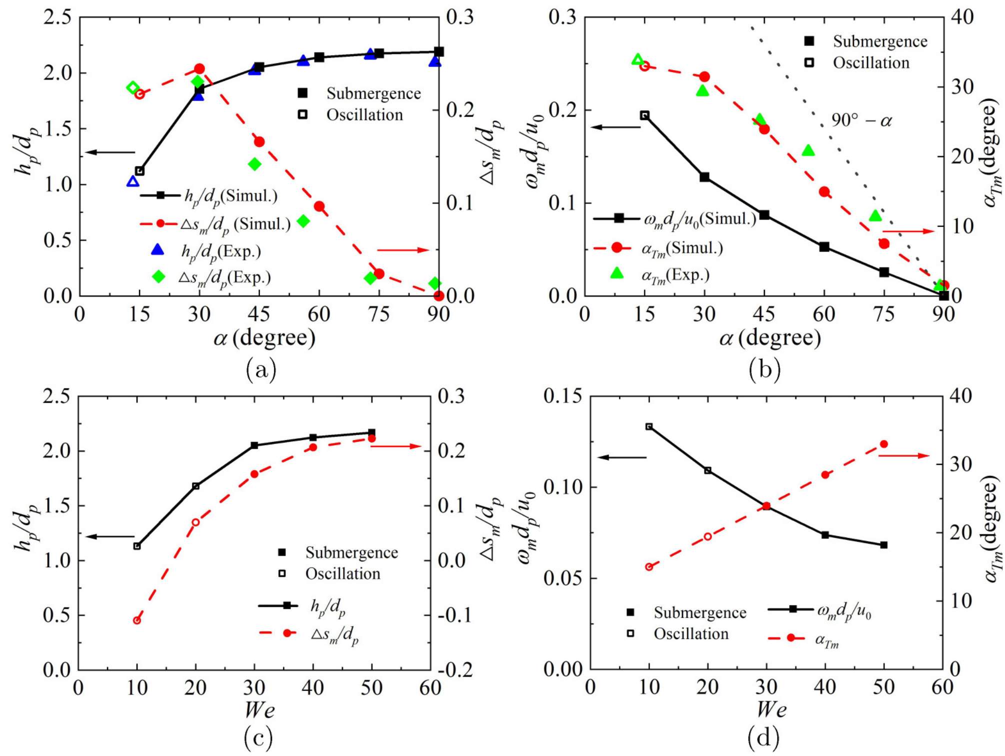

FIG. 5. (a), (c) The penetration depth (h_p) and maximum trajectory deviation (Δs_m) of the particle and (b), (d) the maximum angular velocity of the particle (ω_m) and maximum inclination of the TPCL plane (α_{Tm}) as functions of (a), (b) α (We = 34, Re = 867) and (c), (d) We ($\alpha = 45^\circ$, Re = 867). The open points and the solid points represent the oscillation mode and the submergence mode, respectively.

variations in the maximum angular velocity of the particles (ω_m) and the maximum inclination of the TPCL plane (α_{Tm}) with We. It shows that the increase in We weakens the rotation of particles during the sinking process and decreases the inclination of the TPCL plane ($90^\circ - \alpha - \alpha_{Tm} = 45^\circ - \alpha_{Tm}$) with respect to the impact direction, which means a smaller wetting nonaxisymmetry.

B. Moment analysis

The particle rotates under the influence of a moment during oblique impact. Here we analyze each of the moment terms on the right side of Eq. (4). The numerical simulations demonstrate that $\boldsymbol{M_s} = \boldsymbol{0}$ throughout the impact process. Theoretical studies by Singh *et al.* [34] also illustrate that the surface tension does not generate a moment no matter where the TPCL is located on the particle surface when the contact angle and surface tension coefficient are constant. Since the fluid pressure on the particle surface [the first term on the right side of Eq. (5)] points towards the particle centroid, it will not cause a moment. $\boldsymbol{M_g} = \boldsymbol{0}$, and thus Eq. (4) can be further reduced to

$$I_p \frac{d\boldsymbol{\omega}}{dt} = \iint \boldsymbol{r} \times \left[\mu(\nabla \boldsymbol{v} + \nabla \boldsymbol{v}^{\mathrm{T}}) \cdot \boldsymbol{n}_s\right] dA, \tag{8}$$

which means that the rotation of the particle is derived only from the moment generated by the shear stress of the fluid (mainly the liquid) on the particle surface. Since the direction of the moment is along the x direction, it is described as M_x.

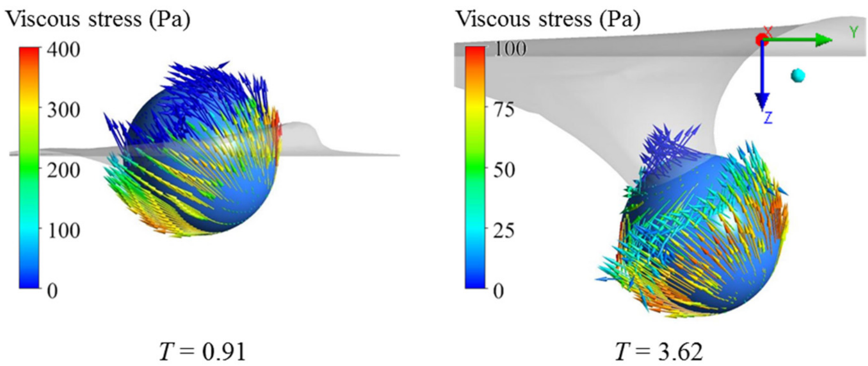

FIG. 6. The shear stress vector distribution on the particle surface at two moments representing the initial and late impact stage (the gray curved surface represents the gas-liquid interface): $\alpha = 43.8^{\circ}$, We = 34, and Re = 867.

Using the impact process with $\alpha = 43.8^{\circ}$, We = 34, and Re = 867 as an example, Fig. 6 shows the vector distribution of the shear stress on the particle surface at two typical moments at the initial and late impact stage, respectively. The shear zone on the particle surface is distributed near the equator that is perpendicular to the velocity direction, and the shear stress on the surface in contact with the gas phase is negligible compared to that on the surface wetted by the liquid. At the beginning of the impact ($T = 0.91$ as an example), the wetting of the particles is nonaxisymmetric and the equator on the left side is first wetted, resulting in a large shear zone below the particle's motion direction, thus generating a clockwise moment. As the particle sinks, the left and right sides of the particle near the equator are both wetted, demonstrating that the shear zone on the particle surface is basically axisymmetric ($T = 3.62$, for example). The clockwise rotation causes the velocity gradient and shear stress on the particle's right side to be greater than those on the left side, which generates an anticlockwise moment.

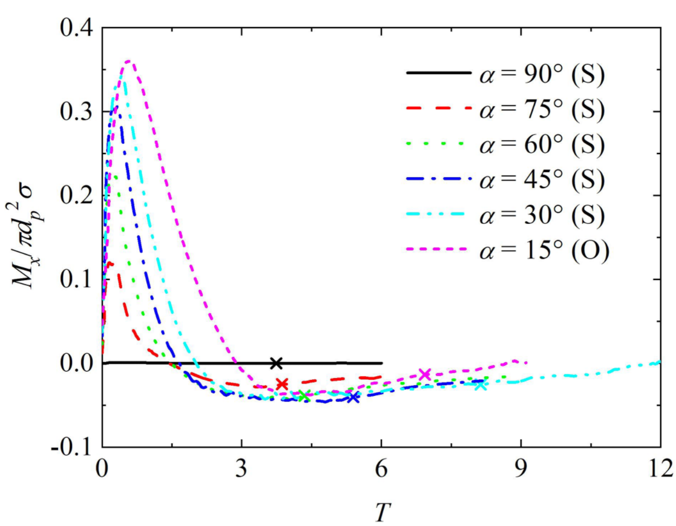

FIG. 7. Time evolution of the moment acting on the particle during impact with different impact angles (× represents the time of particle submergence): We = 34 and Re = 867.

Figure 7 gives the time evolution of the moment acting on the particle during impact with different impact angles. It shows that the moment acting on the particles in the initial impact stage is positive (clockwise) and increases rapidly and then decreases gradually. The moment becomes negative (anticlockwise) at the late stage, and its value is much less than the maximum positive value in the initial stage. This causes the particle to rotate clockwise after impact with an angular velocity first increasing rapidly and then slowly decreasing [as shown in Fig. 3(b)]. Since the nonaxisymmetry of the particle wetting (and the shear stress distribution) increases as α decreases, the positive moment acting on the particle in the initial impact stage is larger and the time duration is longer. Thus the particle's angular velocity during the oblique impact increases significantly with the decrease in α [as shown in Fig. 5(b)]. Also, the nonaxisymmetry of the particle wetting (and the shear stress distribution) decreases as We increases, making the positive moment acting on the particle smaller and thus the rotation of the particle during the oblique impact weaker [as shown in Fig. 5(d)].

C. Force analysis

Unlike the vertical impact, the fluid force $\boldsymbol{F_f}$ contains a Magnus force term $\boldsymbol{F_m}$ caused by the particle's rotation during oblique impact. When a rotating spherical particle moves in a single-phase fluid, the Magnus force acting on it can be expressed as $\boldsymbol{F_m} = C_m\pi\rho_l {d_p}^3 \boldsymbol{\omega} \times \boldsymbol{u}/8$ [35], which is adopted herein to evaluate the Magnus force during oblique impact. Comparing the Magnus force with the surface tension force $\boldsymbol{F_s}$ and hydrodynamic force $\boldsymbol{F_h}$ results in

$$\frac{F_m}{F_s} \sim \frac{C_m\pi\rho_f d_p^3 \omega u/8}{\pi d_p \sigma} \sim \frac{C_m}{8}\mathrm{We}_u \omega d_p/u, \tag{9}$$

$$\frac{F_m}{F_h} \sim \frac{C_m\pi\rho_f d_p^3 \omega u/8}{C_h\pi\rho_f d_p^2 u^2/8} \sim \frac{C_m}{C_h}\omega d_p/u, \tag{10}$$

where C_m is the Magnus force coefficient when the Re is large. Values of C_m proposed by different researchers range from 0.25 to 0.55 [36–38]. We_u is the instantaneous Weber number ($\mathrm{We}_u = \rho_l u^2 d_p/\sigma < \mathrm{We}$). Setting the impact process as $\alpha = 43.8^\circ$, We $= 34$, and Re $= 867$ as an example, we assume $C_h = 1$, and the maximal magnitude $|\boldsymbol{F_m}|$ is less than 10% of the maximum $|\boldsymbol{F_s}|$ and less than 5% of the maximum $|\boldsymbol{F_h}|$. Therefore $\boldsymbol{F_m}$ is negligible compared to $\boldsymbol{F_s}$ and $\boldsymbol{F_h}$. The thick solid line and thin solid line in Fig. 3(a) represent the particle trajectories calculated by adopting the slip velocity boundary condition [Eq. (7)] and nonslip velocity boundary condition on the particle wall surface, and correspond to situations with and without considering particle rotation, respectively. They almost completely overlap each other before the particle is submerged, which indicates that the particle's rotational motion has little effect on its translational motion. $\boldsymbol{F_m}$ is not the cause of the deviation of the particle trajectory.

Since the buoyancy can also be safely neglected compared to $\boldsymbol{F_s}$ and $\boldsymbol{F_h}$, the fluid force $\boldsymbol{F_f}$ is represented by the hydrodynamic force $\boldsymbol{F_h}$ [23]. Using the impact process of $\alpha = 43.8^\circ$, We $= 34$, and Re $= 867$ as an example, Fig. 8(a) shows the time evolution of the components in the y and z directions of $\boldsymbol{F_h}$, $\boldsymbol{F_s}$, and $\boldsymbol{F_t}$ (the total external force acting on the particle). Figure 8(b) shows the time evolution of their inclination angles α_{Fh}, α_{Fs}, and α_{Ft} with respect to the horizontal plane. $\boldsymbol{F_h}$ and $\boldsymbol{F_s}$ dominate the initial and late stages of the oblique impact process. $\boldsymbol{F_h}$ increases rapidly after the particle contacts the liquid surface, while $\boldsymbol{F_{hz}}$ increases faster and reaches a peak earlier than $\boldsymbol{F_{hy}}$. The fluid pressure distribution around the particle at $T = 0.09$ in Fig. 9 shows that the TPCL plane is almost horizontal, causing the high-pressure region at the bottom of the particle to be nonaxisymmetric along the velocity direction. Therefore $|\boldsymbol{F_{hz}}| > |\boldsymbol{F_{hy}}|$ in the very initial impact stage. The direction of the hydrodynamic forces deviates upward with respect to the velocity direction, that is, $\alpha_{Ft} > \alpha_u$, and thus the particle trajectory has a small upward deviation in the very initial impact stage. At a period after the hydrodynamic force reaches its peak, F_h begins to decrease, and the decrease in F_{hy} is much slower than F_{hz}. A low-pressure zone appears on the left side of

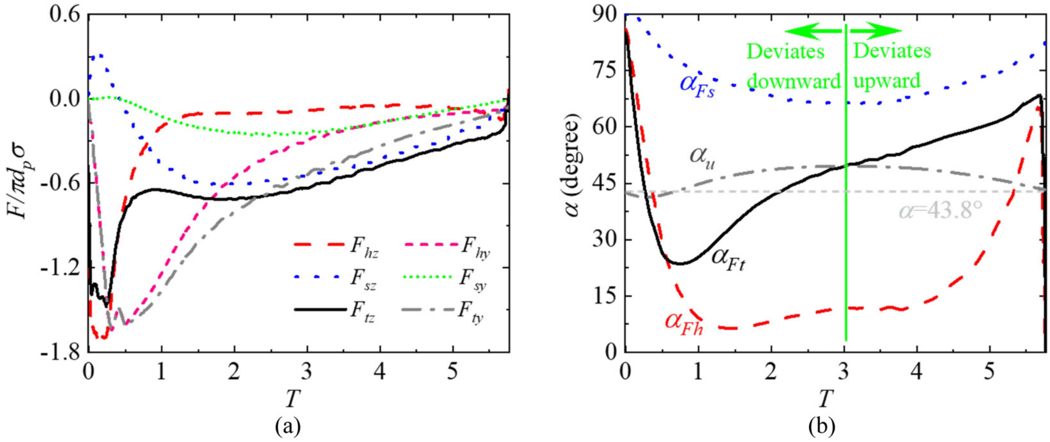

FIG. 8. Time evolution of the magnitude (a) and direction (b) of the forces acting on the particle during impact: $\alpha = 43.8^\circ$, We = 34, and Re = 867.

the particle first ($T = 0.91$ in Fig. 9) since this part is wetted first, causing $|\boldsymbol{F_{hz}}| < |\boldsymbol{F_{hy}}|$ and the direction of the hydrodynamic force to deviate downward with respect to the velocity direction, that is, $\alpha_{Ft} < \alpha_u$. Therefore the particle's trajectory deviates downward. The nonaxisymmetric wetting of the particles also causes the direction of the surface tension force to deviate upward with respect to the velocity direction, that is, $\alpha_{Fs} < \alpha_u$. This decelerates the particle's downward trajectory deviation and makes it even deviate upward at the late impact stage where the surface tension force becomes dominant.

Figures 10(a) and 10(b) present the time evolutions of the components parallel ($F_{//}$) and perpendicular ($F_{//}$) to the particle's impact direction of the acting forces when We = 34, Re = 867, and α equals 60° and 30°, respectively. A positive $F_{//}$ indicates the impact direction, and a positive $F_{\perp}$ demonstrates the upward direction perpendicular to the impact direction. This shows that the peak value of $F_{h//}$ at the initial impact stage decreases, and the peak appears later with the decrease in α. The inclination of the impact direction significantly reduces the slamming force acting on the particle at the initial impact stage. The evolution of $F_{s//}$ during oblique impact is similar to

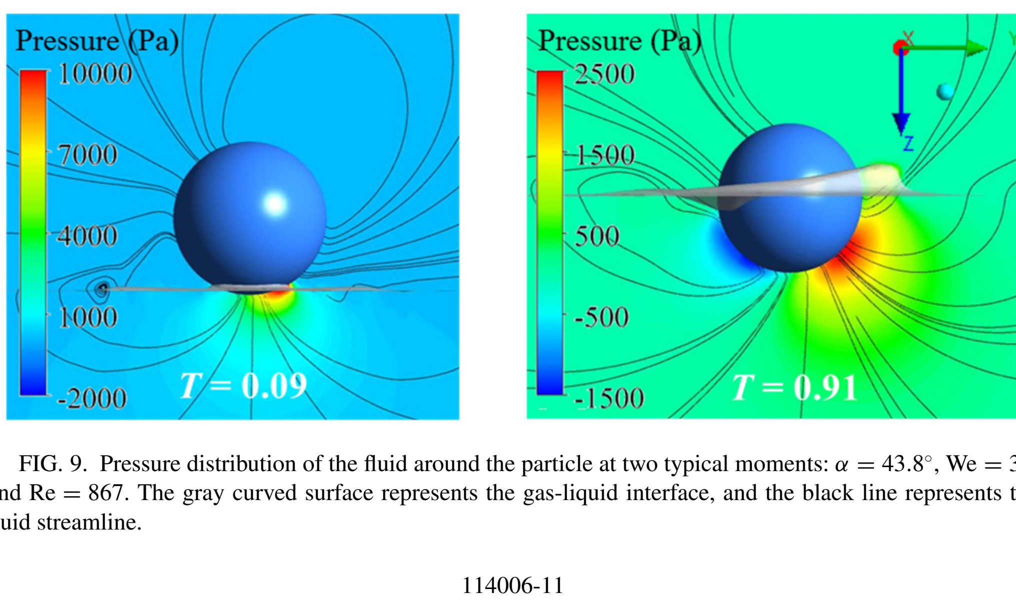

FIG. 9. Pressure distribution of the fluid around the particle at two typical moments: $\alpha = 43.8^\circ$, We = 34, and Re = 867. The gray curved surface represents the gas-liquid interface, and the black line represents the fluid streamline.

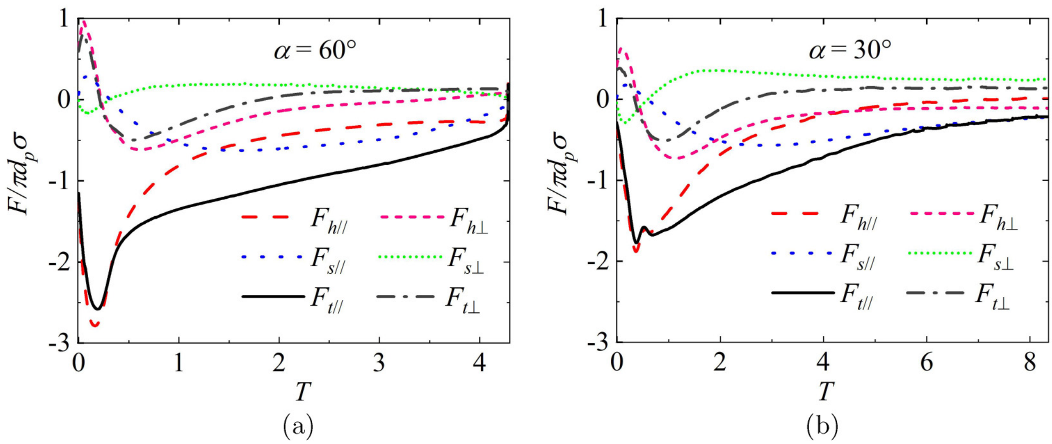

FIG. 10. The time evolution of the components parallel ($_{//}$) and perpendicular ($\perp$) to the impact direction of the hydrodynamic force F_h, surface tension force F_s, and total external force F_t at different impact angles (We = 34 and Re = 867): (a) $\alpha = 60^\circ$ and (b) $\alpha = 30^\circ$.

that during vertical impact. With the decrease in α, the nonaxisymmetry of the particle wetting increases, causing $F_{s//}$ to decrease. Therefore the component in the impact direction of the external force $F_{t//}$ decreases with the decrease in α, which results in a smaller particle deceleration. $F_{s\perp}$ is downward first and then becomes upward during impact, while the evolution of the direction of $F_{h\perp}$ is the opposite. The increase in the nonaxisymmetry of the particle wetting increases both the upward $F_{s\perp}$ and downward $F_{h\perp}$, and the increase in $F_{h\perp}$ is greater in comparison. This makes $F_{t\perp}$ deviate downward after the very initial impact stage and increases with the decrease in α, and the deviation of the particle trajectory also increases with the decrease in α [as shown in Fig. 5(a)]. Though the increase in We decreases the nonaxisymmetry of the particle wetting during oblique impact, the larger particle velocity (or fluid inertia) significantly enlarges the nonaxisymmetric fluid pressure acting on the particle surface during the whole impact process (and also penetration depth for oscillation particles), finally increasing the particle's downward trajectory deviation. For small We impact, the particle does not have enough kinetic energy to enter the stage where a downward force appears and thus shows an upward trajectory deviation finally [as shown in Fig. 5(c)].

IV. CONCLUSIONS

In this study, a three-dimensional numerical method was developed to study the oblique impact of micron particles on liquid surfaces, providing detailed information regarding flow field, acting forces and moment evolutions, and particle motions such as rotation during oblique impact, which is difficult to obtain experimentally. The numerical results accurately reproduced the particle motion and gas-liquid interface evolution at different impact angles. We highlighted how the particle's nonaxisymmetric wetting during oblique impact makes the impact dynamics different from that of vertical impact, and illustrated the effects of impact angle and Weber number on the particle's impact behavior.

Differing from vertical impact, the TPCL plane is not perpendicular to the particle's motion direction during oblique impact but inclines to the horizontal surface, making the wetting of the particle surface nonaxisymmetric along the motion direction. The particle's nonaxisymmetric wetting makes the distributions of the pressure and shear stress on the particle surface nonaxisymmetric, thus changing the forces and moments acting on the particle. On the one hand, the particle is subjected to a viscous moment, which results in a topspin with an angular velocity that first increases and then decreases. On the other hand, the dominant forces at early and late impact stages, i.e., hydrodynamic force and surface tension force, have downward and upward components perpendicular to the impact direction, respectively, causing the particle's downward trajectory to deviate from the impact direction. The Magnus force generated by the rotation is negligible compared to the hydrodynamic force and surface tension force and thus does not affect the particle's translational motion. The particle's nonaxisymmetry wetting increases with decreasing α. Therefore the smaller the α, the smaller the slamming force; the smaller the component of the hydrodynamic force and surface tension parallel to the motion direction, the larger their component perpendicular to the motion direction, resulting in a smaller deceleration and a larger trajectory deviation; a larger viscous moment results in a larger rotation angular velocity. The increasing We weakens the particle's rotation due to the larger nonaxisymmetry wetting and increases the particle's trajectory deviation due to the increasing role of fluid inertia. These findings could improve our understanding of the nonaxisymmetric impact behavior of micron particles on liquid surfaces and provide guidance for the modeling and prediction of particle oblique impact behaviors.

ACKNOWLEDGMENT

This work was supported by funding from the National Natural Science Foundation of China (Grant No. 51576109).

[1] S. Ashley, Warp drive underwater, Sci. Am. **284**, 70 (2001).

[2] T. Truscott, A. Techet, and D. Beal, Shallow-angle water entry of ballistic projectiles, Bull. Am. Phys. Soc. **53**(15), BAPS.2008.DFD.AK.2 (2008).

[3] T. Von Karman, The impact on seaplane floats during landing, Technical Report Archive & Image Library (1929).

[4] H. Wagner, Phenomena associated with impacts and sliding on liquid surfaces, Z. Angew. Math. Mech. **12**, 193 (1932).

[5] J. W. M. Bush and D. L. Hu, Walking on water: Biolocomotion at the interface, Annu. Rev. Fluid Mech. **38**, 339 (2006).

[6] D. L. Hu, B. Chan, and J. W. M. Bush, The hydrodynamics of water strider locomotion, Nature (London) **424**, 663 (2003).

[7] B. Ji, Q. Song, and Q. Yao, Limit for small spheres to float by dynamic analysis, Langmuir **34**, 10163 (2018).

[8] B. Ji, Z. Tang, Q. Song, Z. Ge, and Q. Yao, Dynamic flotation conditions for elongated cylinders on liquid surfaces, J. Colloid Interface Sci. **547**, 87 (2019).

[9] S. Mitra, E. Doroodchi, V. Pareek, J. B. Joshi, and G. M. Evans, Collision behaviour of a smaller particle into a larger stationary droplet, Adv. Powder Technol. **26**, 280 (2015).

[10] G. Kaptay, Interfacial phenomena during melt processing of ceramic particle-reinforced metal Matrix composites, Part II. Interfacial force between a spherical particle and an approaching solid/liquid interface, Mater. Sci. Forum **215–216**, 467 (1996).

[11] A. Wang, Q. Song, and Q. Yao, Behavior of hydrophobic micron particles impacting on droplet surface, Atmos. Environ. **115**, 1 (2015).

[12] S. Zhu, R. Liu, T. Wang, Y. Niu, H. Lu, and X. Chen, Penetration time of hydrophilic micron particles impacting into an unconfined planar gas-liquid interface, Chem. Eng. Sci. **193**, 282 (2019).

[13] B. Ji, Q. Song, and Q. Yao, Impact of hydrophobic micron ellipsoids on liquid surfaces, J. Colloid Interface Sci. **532**, 711 (2018).

[14] T. T. Truscott, B. P. Epps, and J. Belden, Water entry of projectiles, Annu. Rev. Fluid Mech. **46**, 355 (2014).

[15] D. M. Kintea, J. Breitenbach, V. T. Gurumurthy, I. V. Roisman, and C. Tropea, On the influence of surface tension during the impact of particles on a liquid-gaseous interface, Phys. Fluids **28**, 12108 (2016).

[16] D. G. Lee and H. Y. Kim, Impact of a superhydrophobic sphere onto water, Langmuir **24**, 142 (2008).

[17] J. M. Aristoff, T. T. Truscott, A. H. Techet, and J. W. M. Bush, The water entry of decelerating spheres, Phys. Fluids **22**, 032102 (2010).
[18] D.G. Lee and H.Y. Kim, Sinking of small sphere at low Reynolds number through interface, Phys. Fluids **23**, 072104 (2011).
[19] H. Ding, B. Q. Chen, H. R. Liu, C. Y. Zhang, P. Gao, and X. Y. Lu, On the contact-line pinning in cavity formation during solid-liquid impact, J. Fluid Mech. **783**, 504 (2015).
[20] H. Chen, H. R. Liu, X. Y. Lu, and H. Ding, Entrapping an impacting particle at a liquid–gas interface, J. Fluid Mech. **841**, 1073 (2018).
[21] O. Verezub, G. Kaptay, T. Matsushita, and K. Mukai, Penetration dynamics of solid particles into liquids high-speed experimental results and modelling, Mater. Sci. Forum. **473**, 429 (2005).
[22] A. Wang, Q. Song, B. Ji, and Q. Yao, In-situ observation of hydrophobic micron particle impaction on liquid surface, Powder Technol. **311**, 408 (2017).
[23] B. Ji, Q. Song, and Q. Yao, Numerical study of hydrophobic micron particle's impaction on liquid surface, Phys. Fluids **29**, 077102 (2017).
[24] B. Ji, Q. Song, A. Wang, and Q. Yao, Critical sinking of hydrophobic micron particles, Chem. Eng. Sci. **207**, 17 (2019).
[25] C. Clanet, F. Hersen, and L. Bocquet, Secrets of successful stone skipping, Nature (London) **427**, 29 (2004).
[26] L. Rosellini, F. Hersen, C. Clanet, and L. Bocquet, Skipping stones, J. Fluid Mech. **543**, 137 (2005).
[27] W. Johnson and S. R. Reid, Ricochet of spheres off water, J. Mech. Eng. Sci. **17**, 71 (1975).
[28] T. Guillet, M. Coux, D. Quéré, and C. Clanet, Path instabilities of streamlined bodies, J. Fluid Mech. **864**, 286 (2019).
[29] B. Ji, Q. Song, K. Shi, J. Liu, and Q. Yao, Oblique impact of microspheres on the surface of quiescent liquid, J. Fluid Mech. **900**, A17 (2020).
[30] H. R. Liu, P. Gao, and H. Ding, Fluid-structure interaction involving dynamic wetting: 2d modeling and simulations, J. Comput. Phys. **348**, 45 (2017).
[31] M. Do-Quang and G. Amberg, Numerical simulation of the coupling problems of a solid sphere impacting on a liquid free surface, Math. Comput. Simulat. **80**, 1664 (2010).
[32] C. W. Hirt and B. D. Nichols, Volume of fluid (VOF) method for the dynamics of free boundaries, J. Comput. Phys. **39**, 201 (1981).
[33] J. U. Brackbill, D. B. Kothe, and C. Zemach, A continuum method for modeling surface tension, J. Comput. Phys. **100**, 335 (1992).
[34] P. Singh and T. I. Hesla, The interfacial torque on a partially submerged sphere, J. Colloid Interface Sci. **280**, 542 (2004).
[35] J. S. Marshall and S. Li, *Adhesive Particle Flow* (Cambridge University Press, Cambridge, England, 2014).
[36] T. Tanaka, K. Yamagata, and Y. Tsuji, Experiment on fluid forces on a rotating sphere and spheroid, Proceedings of the 2nd KSME-JSME Fluids Engineering Conference **1**, 366 (1990).
[37] B. D. Tri, B. Oesterle, and F. Deneu, Premiers resulats sur la portance d'une sphere en rotation aux nombres de Reynolds intermediaies, C. R. Acad. Sci., Ser. H **311**, 27 (1990).
[38] P. Bagchi and S. Balachandar, Effect of free rotation on the motion of a solid sphere in linear shear flow at moderate Re, Phys. Fluids **14**, 2719 (2002).